

<https://doi.org/10.1038/s42005-024-01558-0>

Genetic algorithm-enhanced microcomb state generation

Check for updates

Celine Mazoukh¹, Luigi Di Lauro¹ ✉, Imtiaz Alamgir¹, Bennet Fischer^{1,2}, Nicolas Perron¹, A. Aadhi^{1,3}, Armaghan Eshaghi⁴, Brent E. Little⁵, Sai T. Chu⁶, David J. Moss⁷ & Roberto Morandotti¹ ✉

Microcavities enable the generation of highly efficient microcombs, which find applications in various domains, such as high-precision metrology, sensing, and telecommunications. Such applications generally require precise control over the spectral features of the microcombs, such as free spectral range, spectral envelope, and bandwidth. Most existing methods for customizing microcomb still rely on manual exploration of a large parameter space, often lacking practicality and versatility. In this work, we propose a smart approach that employs genetic algorithms to autonomously optimize the parameters for generating and tailoring stable microcombs. Our scheme controls optical parametric oscillation in a microring resonator to achieve broadband microcombs spanning the entire telecommunication C-band. The high flexibility of our approach allows us to obtain complex microcomb spectral envelopes corresponding to various operation regimes, with the potential to be directly adapted to different microcavity geometries and materials. Our work provides a robust and effective solution for targeted soliton crystal and multi-soliton state generation, with future potential for next-generation telecommunication applications and artificial intelligence-assisted data processing.

The discovery of optical frequency combs in the late 1990s by Hall and Hänsch¹ has since contributed to widespread technological developments in fundamental and applied research areas, in both classical^{2–7} and quantum domains^{8–11}. Unlike traditional schemes for comb generation that require bulky and expensive systems^{12–14}, microcombs, produced in optical microcavities^{3,15–17}, (e.g., microdisks, microring resonators (MRRs), or photonic crystals), represent a stable and compact alternative. Microcombs arise by exploiting the nonlinear interactions of the injected optical field with the material composing their structure. Such nonlinear optical processes, including optical parametric conversion^{18–23}, are mediated by the strong modal confinement due to the reduced dimensions of the waveguide and can thus produce a broad spectrum with high conversion efficiency^{15,17}. This aspect makes them suitable for a variety of out-of-the-lab applications, such as for light detection and ranging (LIDAR)²⁴, chip-scale atomic clocks²⁵, portable sensors²⁶, as well as for application towards photonic artificial intelligence-assisted data processing^{4,27,28}, enabling new smart applications for the Internet of Things and the forthcoming industry 4.0 revolution²⁹.

In the domain of microcomb-based telecommunication, microcombs have been applied, e.g., as optical filters³⁰ and for on-chip wavelength division multiplexing enabling high-capacity data transmission^{17,31–33}. Spectral

instability and uneven power distribution in the comb lines decrease the communication performance, resulting in degraded signal quality and reduced efficiency, which affects data transfer rates and available bandwidth³⁴. Therefore, precise control of the microcomb's spectral envelope is required to comply with the performance demands of such applications.

Different solutions to this hurdle have been proposed, including active or passive schemes. For example, frequency stabilization, involving external reference lasers and phase-lock loops¹⁸, multipumping schemes³⁵, electro-optical modulation³⁶, or self-injection locking³⁷, have been developed to tailor and stabilize the microcomb features. Passive frequency stabilization, including detuning scanning³⁵ and filter-driven four-wave mixing^{6,38}, also represents a valid alternative to control the output frequency of the microcomb. However, these advanced techniques still encounter several challenges.

Achieving and maintaining the desired output characteristics of the microcomb requires the attainment of the appropriate dynamical regime that allows their stable formation, in turn necessitating precise control over the set of accessible experimental parameters, which can be demanding due to the nonlinear behavior of the MRRs³⁹. Thus, a smart, efficient, and reliable

¹Institut national de la recherche scientifique (INRS-EMT), Varennes, Canada. ²Leibniz Institute of Photonic Technology, Jena, Canada. ³Centre for Nanophotonics, Physics, Engineering Physics & Astronomy, Queen's University, Kingston, Canada. ⁴Huawei Technologies Canada, Markham L3R 5A4, Canada. ⁵QXP Technologies, Inc., Xi'an, China. ⁶City University of Hong Kong, Hong Kong, China. ⁷Optical Sciences Centre, Swinburne University of Technology, Hawthorn, Australia.

✉ e-mail: luigi.dilauro@inrs.ca; roberto.morandotti@inrs.ca

approach that can autonomously search for and locate the optimal parameters to obtain microcombs with the targeted features is highly needed. This task represents a global optimization problem⁴⁰, which can generally be tackled with different regularization techniques⁴¹, as well as with more advanced smart optimization algorithms, such as gradient descent, particle swarm optimization⁴², or genetic algorithms (GAs)⁴³, among others.

GAs are a class of metaheuristic optimization algorithms inspired by the principles of natural selection and evolution investigated in biology⁴⁴. They have been employed in diverse multiparameter global optimization problems across different areas of physics and engineering, including parameter estimation⁴⁵, image reconstruction⁴⁶, and tomography⁴⁷. In recent years, GAs have shown immense potential in the domain of smart photonics, particularly for inverse design problems relating to the development of new photonic systems and devices with optimized operation, such as the microcomb-to-geometry inverse design of microcavities^{48–51} and photonic crystals design with engineered dispersion⁵². They have also been applied towards experimental optimization, such as for increasing the conversion efficiency of dispersive wave generation⁵³. In contrast to conventional gradient-based optimization algorithms⁴¹, GAs are highly effective in problems where the model that describes the system dynamics is non-linear or unknown, yielding a parameter space that exhibits multiple local minima and even discontinuities, for which gradient-based approaches often fail. As such, they have been demonstrably useful for problems that arise in smart photonics applications, where targeting specific operating regimes is paramount, yet the quality and stability of solutions are dependent on a complex multi-dimensional space of cavity parameters, such as on-chip pulse tailoring⁴², soliton⁵⁴, and supercontinuum optimization^{55,56}, as well as extremum seeking for laser mode-locking^{57–59} and self-driving lasers⁶⁰.

In this work, we propose a smart scheme for autonomous and optimized control of microcomb regimes in an integrated MRR to tailor the cavity output. Using microcomb features such as line spacing, intensity

envelope, and intracavity power as targets, we employ GAs to find the optimal set of experimental parameters corresponding to the desired intracavity dynamics controlling microcomb formation. We generate a wide range of microcombs corresponding to distinct dynamical regimes through simple modification of the GA, including modulation instability (MI)^{15,61} and soliton crystal (SC) regimes^{4,62}, in turn demonstrating the reconfigurability of our scheme.

Results

Principle of operation

The experimental setup used for microcomb generation and tailoring is shown in Fig. 1a. A continuous-wave laser (CWL) serves as the optical source and is coupled to a temperature-controlled integrated MRR (doped silica glass waveguide with a free spectral range (FSR) of 48.9 GHz⁶³, see Methods section). The optical output signals are collected at the drop port, using an optical spectrum analyzer (OSA) and a power meter (PM).

The CWL output intensity is boosted with an erbium-doped fiber amplifier (EDFA) to pump the MRR around the center frequency of 193.4 THz, which triggers Kerr microcombs through cascaded degenerate four-wave mixing processes⁶⁴. When the intracavity power is sufficiently high, mode-crossing between orthogonal modes from different families emerges due to geometrical imperfections and high field confinement as we detune the pump with respect to the center frequency, allowing different degenerate modes to exchange energy¹⁵. This, in turn, leads to broadband microcombs, whose spectra can fill the entire telecom C-band⁶⁴. However, to trigger this mechanism, a simultaneous fine-tuning of several setup parameters is required to control such nonlinear processes. To this end, we implement a scheme interfacing the setup components with a genetic algorithm (GA), which controls the laser scan parameters and optimizes the output, as represented in Fig. 1b.

The parameters defining the properties of the microcombs are contained in a vector \mathbf{P}_i^n , which is referred to as an i -th individual of the n -th generation in the GA formulation. A set of S individuals comprises a population \mathbf{X}^n at a given step n of the evolution, with their respective parameters, p_{ij} , also referred to as genes:

$$\mathbf{X}^n = \begin{bmatrix} \mathbf{P}_1^n(p_{11}, p_{12}, p_{13}, p_{14}, p_{15}) \\ \mathbf{P}_2^n(p_{21}, p_{22}, p_{23}, p_{24}, p_{25}) \\ \vdots \\ \mathbf{P}_S^n(p_{S1}, p_{S2}, p_{S3}, p_{S4}, p_{S5}) \end{bmatrix} \quad (1)$$

In our case, there are five genes corresponding to tunable parameters of the setup, comprising the center frequency of the pump, ω_0 , frequency span of the sweep, $\Delta\omega_0$, sweep step size, $d\omega$, and dwell time, dt , as well as the EDFA current setting I .

After initializing the algorithm, the boxed steps shown in Fig. 1b are applied iteratively for each individual in the population: the parameters are passed on to the experimental setup to initiate the comb generation, and the corresponding MRR output is collected in the form of the optical spectrum and power trace. The output is then passed on to the fitness evaluation phase, where it is assigned a score according to its proximity to the target microcomb shape. The fitness function F assigns a score to the candidate individuals, which we define as a weighted sum of our microcomb shape-related objectives f_i

$$F = \sum_i^N f_i w_i, \quad (2)$$

in which each f_i is a metric measuring the discrepancy between the MRR output and the individual target microcomb features (see Methods section). The choice of the weight values w_i to be used in Eq. (2) is empirically found and made once, prior to running the algorithm.

Once the fitness of every individual in the population \mathbf{X}^n is evaluated in step n of the GA, a subset of the best individuals is selected to compose a new

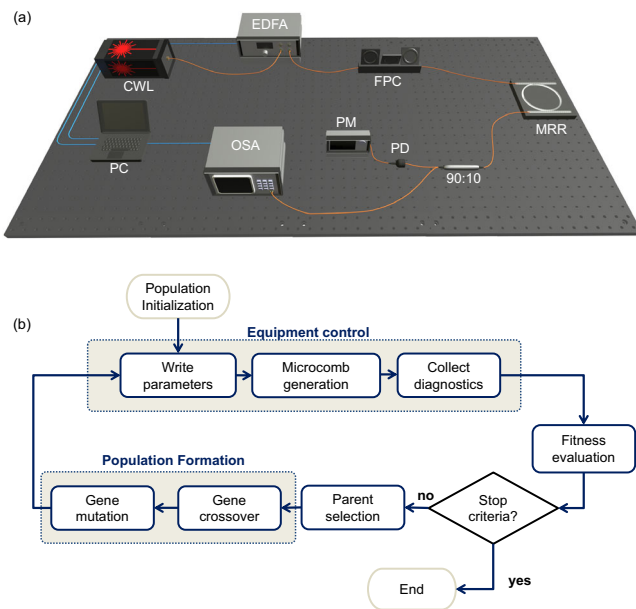


Fig. 1 | Smart microcomb generation scheme. **a** Experimental setup for microcomb generation and tailoring in a microresonator. CWL continuous-wave laser, EDFA erbium-doped fiber amplifier, FPC fiber polarization controller, MRR microring resonator, PD photodiode, PM power meter, OSA optical spectrum analyzer, PC personal computer. CWL, EDFA, OSA, and PM are controlled remotely and interfaced with the genetic algorithm (GA) to set the experimental parameters. **b** Operation scheme to implement our GA for microcomb generation. The highlighted steps are applied iteratively for all individuals of the population in the Equipment Control phase and for all selected individuals of the Population Formation phase.

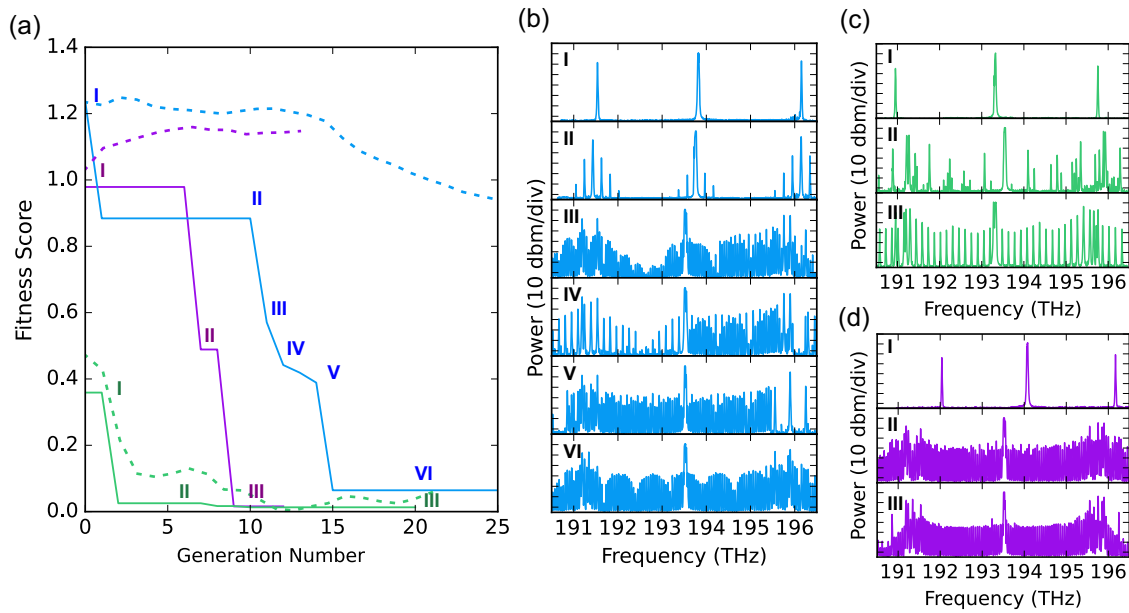


Fig. 2 | Convergence of the genetic algorithm towards target microcomb. a Convergence plots for three separate realizations of the genetic algorithm (GA) that show the fitness score improvement as the generation number increases, eventually converging to better values. Dotted lines depict the average fitness score corresponding to each realization of the GA, while solid lines represent the best score within each generation. The line colors—blue, green, and purple—correspond to the microcombs displayed in **b–d**, respectively. **b–d** Spectral output at the labeled points

of each convergence plot. Each drop in the convergence plots in **a** shows a progress in refining the output microcombs (**b–d**), enabling us to observe the improvement in intermediate microcomb states, as we approach the desired target. The GA realization corresponding to **c** was initiated with a better gene pool compared to **b** and **d**. Hence, the corresponding average fitness plot in **a** achieves overall lower values compared to the others.

population \mathbf{X}^{n+1} in the next step $n+1$. Each individual in the new population contains parameters chosen from a pair of these (best-selected) individuals, through crossover **C** and mutation **M**, operations forming what is known as offspring according to the GA formulation⁴⁰. The operator **C** uniformly mixes the genes from two selected individuals, \mathbf{P}_l^n and \mathbf{P}_m^n , following a uniform probability distribution $D \in [0,1]$. The mutation operator **M** then introduces a probability that any one (or more) of these genes would change to a random value within the gene boundaries. The two operators respectively act according to:

$$C(\mathbf{P}_l^n, \mathbf{P}_m^n)_k = \bar{p}_{kj}^{n+1} = \begin{cases} p_{lj}^n & \text{if } D_j \leq 0.5 \\ p_{mj}^n & \text{if } D_j > 0.5 \end{cases}, \quad l, m = 1 \dots S; j = 1 \dots 5, \text{ with } l \neq m, \quad (3)$$

$$M(\bar{\mathbf{p}}_k^{n+1})_k = p_{kj}^{n+1} = \begin{cases} p_{kj}^* & \text{if } r_j \leq M_r \\ \bar{p}_{ij}^{n+1} & \text{if } r_j > M_r \end{cases}, \quad i = 1 \dots S; j = 1 \dots 5 \quad (4)$$

in which \bar{p}_{kj}^{n+1} is the j -th gene of the k -th offspring generated from crossover operation prior to mutation, while p_{kj}^{n+1} is the gene after mutation. r_k is a uniformly distributed random number, while M_r is the mutation rate. The random values p_j^* are, in turn, selected from a uniform distribution, whose lower and upper limits are given by the gene boundaries (see the subsection “Genetic algorithm parameters” in the Methods Section for more details).

These two operations allow the parameter space to be explored beyond the current population such that, over many iterations, the algorithm can access different dynamical regimes for microcomb formation by trying various combinations of laser frequency scan settings and intracavity power. We also implement an elitism mechanism, in which the best-performing individual in a population is retained as-is to the next generation.

The process of collecting and evaluating the MRR output is repeated for every individual of the new population until the defined stopping criteria is reached. In our implementation, the algorithm stops after no improvement in the fitness score is observed for ten consecutive generations, indicating that the algorithm has converged to a minimum of the fitness function.

Targeting microcombs

We apply our scheme to target different microcomb spectral envelopes corresponding to different regimes, such as primary combs, MI microcombs, and dissipative Kerr solitons, including SCs. Fig. 2 shows the performance of the GA: Fig. 2a reports the convergence plots for three such GA realizations with different targets, depicting the best and average fitness score per generation as the algorithm progresses, while Fig. 2b–d display the corresponding microcomb shapes at each of the points of improvement in the convergence plots. We note that the number of iterations required to obtain the target spectrum depends on the microcomb state; however, in the realizations we report here, we achieved convergence after around 20 generations.

In the case corresponding to Fig. 2b, we set the line spacing of the target microcomb to the MRR’s fundamental FSR (48.9 GHz) and the spectral envelope to an absolute sinusoidal shape, obtaining primary and secondary comb line formation. The latter process can be associated with the presence of cavity multi-solitons as it has been widely demonstrated^{62,65–68}. The other two realizations of the GA reported in the convergence plot correspond to target microcombs defined by a line spacing of ~150 GHz (3 FSR) in Fig. 2c, resembling a MI microcomb, and a line spacing of 48.9 GHz in Fig. 2d, with minimized intensity variations among its frequency lines and the signature step in intracavity power, corresponding to SC formation^{4,62}.

As shown in Fig. 2, the fitness scores are initially higher, corresponding to off-resonance laser scan parameters. All three realizations exhibit a significant drop in the convergence plot occurring around generation 5, reflecting the fact that the worst genes in the initial population are quickly ‘bred out’, since better genes have a higher probability of being selected. With continued evolution, the algorithm traverses the landscape of the parameter space with successive iterations, yielding a better score, resulting in the general descending trend in Fig. 2a. For the case represented by the blue line, corresponding to the microcomb in Fig. 2b, the convergence plot shows a flat region after the initial drop, where the algorithm is converging to a local minimum. Around generation 17, however, mutations have introduced enough variation in the individuals’

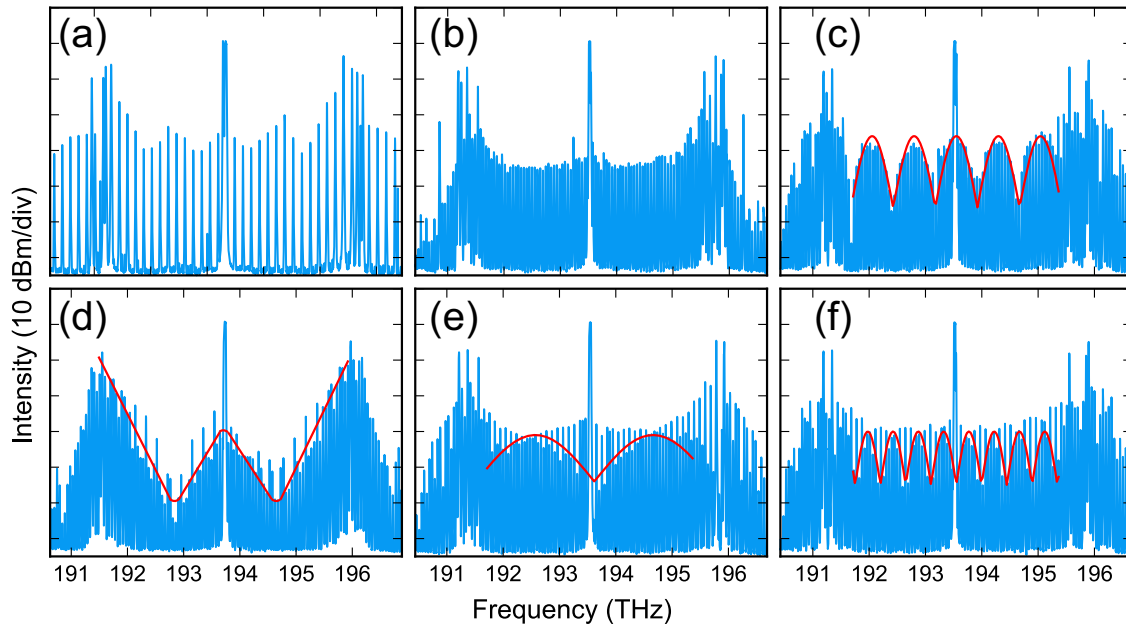


Fig. 3 | Customization of various microcomb regimes. Gallery of microcombs achieved via the genetic algorithm (GA) by setting constraints on line spacing and spectral envelope: Targeting, **a** a line spacing of ~ 150 GHz (≈ 3 FSR), **b** a line spacing of 48.9 GHz (≈ 1 FSR) and minimized intensity variance (± 3 dBm), and **c–f** a line

spacing of 48.9 GHz and desired spectral envelopes (solid red lines). The variety of microcombs achieved demonstrates the GA’s ability to search for and locate optimal spectral features as specified by the objectives.

parameters to locate a better solution corresponding to a lower minimum, as evident in the second more significant drop in the convergence plot. The corresponding traces at each point I–VI in Fig. 2b illustrate the GA’s findings during this search: II is when more comb lines first start to appear, yielding a substantial improvement in the line spacing requirement, hence the large drop in the convergence plot. Point III, then, is the first sign of more complex dynamics as seen in the spectral envelope, with the line spacing reaching the 48.9 GHz target, reflecting the drop in the convergence plot. However, such a state is unstable, as the asymmetric shape shows. Minor improvements with respect to stability and envelope are achieved between III and V as seen in Fig. 2a, until at point VI the desired sinusoidal spectral envelope shape is achieved, leading to the final drop in the convergence plot. This is reflected in the quality of the spectrum shown in Fig. 2b. Fitness evaluation is detailed in the Methods section.

Similarly, we can visually track the progression of the GA for the other two realizations. For the case corresponding to Fig. 2c, the associated (green) plot in 2 (a) converges in fewer generations, as only a single objective is defined in the fitness function: a target line spacing of ~ 150 GHz. In Fig. 2d we search for a SC with the characteristic flat spectrum shape reported in the literature^{4,5}. We target such a state by requiring a line spacing of 48.9 GHz (MRR FSR), a criterion to minimize intensity variations of the comb lines, in addition to the characteristic SC step in the transmitted power trace. The evolution of the optical trace along the corresponding convergence plot shows that the GA quickly

locates a microcomb that satisfies the line spacing criterion, then fine-tuning takes place, decreasing the intensity variations to ± 3 dBm in the C-band. The flat spectrum is achieved by imposing a large weight on the intensity variation criterion in the fitness function, as represented by the marked drop between II and III in the convergence plot.

Following this principle for which the algorithm can converge to better solutions over generations, our GA can explore a rich landscape of different dynamical regimes for microcomb formation. Figure 3 shows a gallery of different microcomb states achieved using our implementation of the GA by simply redefining the objectives f_i in the fitness function (Eq. 2) to describe the target microcomb in terms of its line spacing, spectral envelope, and average intracavity power. Table 1 shows the parameters found by the GA to yield the corresponding subfigures shown in Fig. 3. The spectral traces determined by the algorithm, as in Fig. 3, illustrate its ability to target distinct line spacings (as in Fig. 3a, e), flatter spectra (as in Fig. 3b), with intensity variation ± 3 dBm in the C-band), as well as explicit spectral envelope definitions (as in Fig. 3c, d, and f), for the generation of distinct microcombs with over 10 THz bandwidth, spanning the entire C-band.

Figure 4 shows each individual’s fitness score as a function of detuning and laser sweep speed in a single GA run. We calculate the laser sweep speed and detuning from the parameters of each individual, that is, $d\omega$ and dt for the former, ω_0 and $\Delta\omega_0$ for the latter. Each plot in Fig. 4a–c corresponds to a different objective in the fitness function, measuring proximity to target line spacing, spectral envelope, and intracavity power, respectively. Fig. 4d shows the weighted sum, that is, the fitness landscape of the parameter space as measured by the fitness function of Eq. (2). This resultant fitness landscape exhibits better contrast between regimes that would otherwise yield similar fitness scores when measured via a single objective, as can be seen when comparing Fig. 4a–c with Fig. 4d. For example, Fig. 4a and b exhibit two regions of similar quality fitness (indicated in the figure with arrows, with a score closer to zero) for two adjacent resonances. Without measuring the power trace (Fig. 4c), the algorithm would incorrectly assume that those two regions yield microcomb states with the same target features (implied by Fig. 4a and b), which would in turn skew the convergence of the algorithm towards sub-optimal solutions. Thus, formulating the fitness function in terms of multiple objectives is imperative to set our GA’s ability to interpret

Table 1 | Parameter list for microcomb tailoring reported in Fig. 3

Fig. 3 panel	ω_{start} (THz)	ω_{stop} (THz)	$d\omega$ (GHz)	dt (s)	I (A)
(a)	193.3148	193.2525	0.1495	0.1	3.60
(b)	193.5159	193.4924	0.3247	0.5	3.96
(c)	193.4928	193.5222	0.2498	0.5	3.90
(d)	193.7286	193.6785	0.0125	0.5	3.66
(e)	193.5309	193.4935	0.1249	0.1	3.51
(f)	193.5159	193.4785	0.2997	0.5	3.90

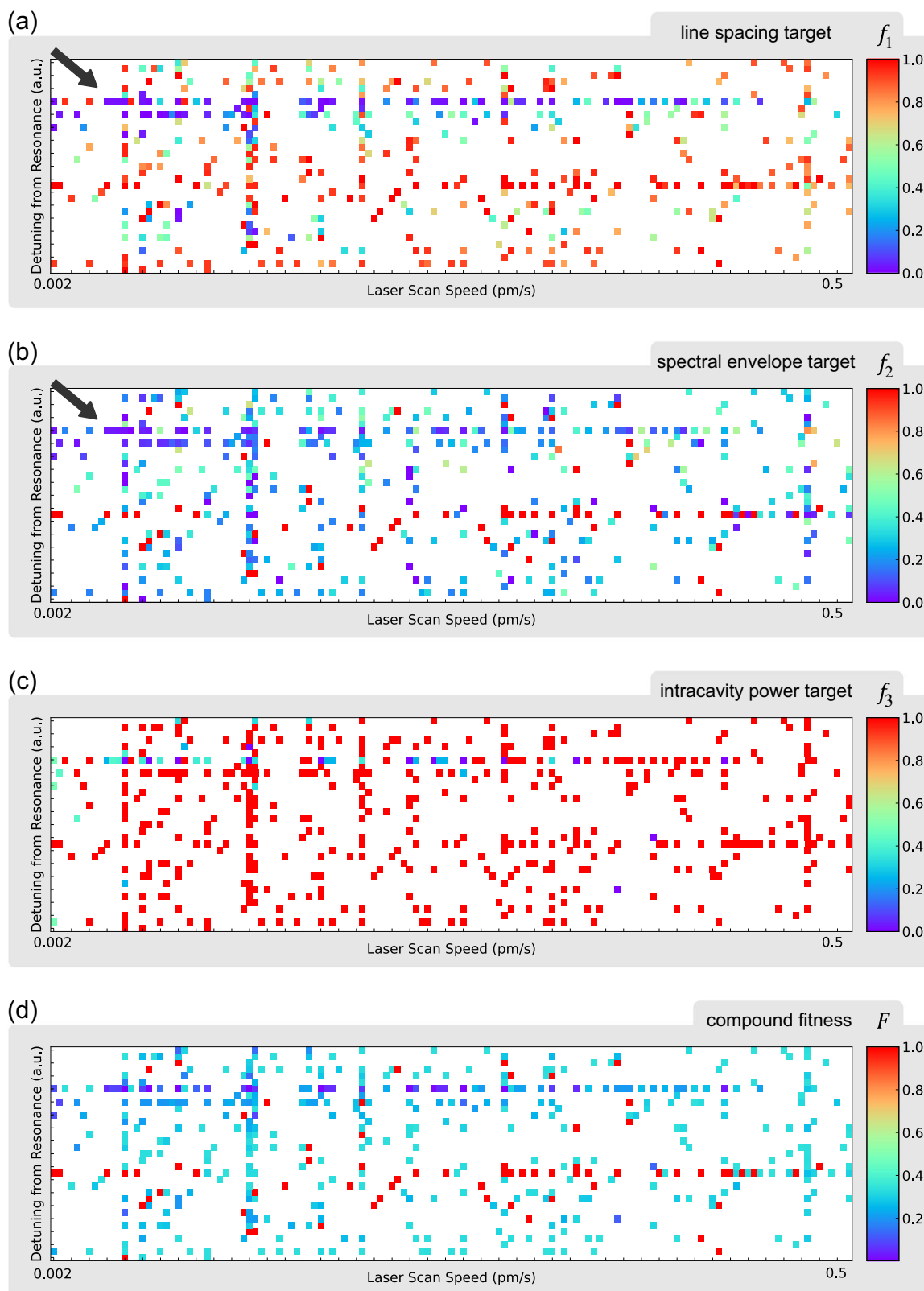


Fig. 4 | Fitness scores for the collected genetic algorithm iterations. **a–c** Scores of individual objectives f_i in the fitness function described in Eq. (2), represented by the scattered plots. **d** Overall fitness function scores comprising the weighted sum of **a–c**. The axes are detuning from the microring resonator cold resonance and laser scan

speed, calculated from the experimental parameters of each individual: ω_0 and $\Delta\omega_0$ for the former, $d\omega$ and dt for the latter. The arrows indicate the regions of optimized solutions (lower score). The color bars of the scattered plots indicate the corresponding objective function score **a–c** and compound fitness value **d**.

and, hence, search for and correctly locate, the target microcomb. The sparsity of the plots in Fig. 4 is due to the GA's exploration of the parameter space being concentrated around the best-performing regions, rather than exhaustively searching the entire space.

We note that the microcomb states accessible by our algorithm are exclusively defined by the fabrication and design properties of the MRR itself (e.g., the dispersion profile of the material, the geometry, etc.). Thus, our GA approach does not alter any of these properties during its application. Rather, it enables intelligent and user-friendly location of the optimal experimental parameters required to access the dynamical regimes allowed by the MRR. For example, one may consider the parameters of the laser frequency scan. Frequency scanning of the pump laser has been established as a method to achieve stable phase-locked states in microcavities that exhibit Kerr and thermal nonlinearities¹⁵. As the pump is tuned into a MRR resonance, the Kerr effect introduces an intensity-dependent contribution to the refractive index, which induces the resonances to drift. At the same time, the strong intensity of the pump field leads to thermo-optical effects, causing the resonator to heat up. This, in turn, produces variations in the temperature-dependent refractive index and alters the optical path length, contributing to the overall drift of resonances¹⁵. In such a scenario, a stable operational regime can be reached by setting the pump frequency above the cold cavity resonance and then approaching it by scanning the pump towards smaller frequencies⁶⁹. Thus, the pump frequency tuning speed is an important parameter affecting the accessibility of microcomb states. For soliton states, in which a loss in intracavity power induces the transition from chaos to a phase-locked regime⁶⁹, the correct speed would allow for losses to be compensated for by the residual resonator heating after the laser scan, thus maintaining the system equilibrium. Hence, the use of GA yields insight into the magnitude of the resonance drift and, when combined with the inclusion of the frequencies defining the start and end point of the scan, allows for the consistent achievement of the same effective detuning for a given microcomb state and by extension, the targeting of stable operational regimes for these microcombs.

Microcomb characterization

We study the validity of our approach by characterizing the microcombs generated using the experimental parameters located by the GA. We measure the spectral coherence of the microcombs across the entire spectrum, using a delayed Mach-Zender interferometer and calculating the visibility V per comb line from the resulting spectral fringes. The visibility of the interference fringes observed at the output of the Mach-Zender interferometer corresponds to the modulus of the (wavelength-dependent) complex degree of the first-order coherence^{70,71}.

In Fig. 5 we reproduce three spectrally distinct microcombs previously located by the GA, related to multi-soliton and SC states. The spectra are superimposed with their associated line-by-line visibility data for three different delays. Fig. 5a–c show delay values of 20 ps, 5 ns, and 15 ns, corresponding to 0.04, 1, and 3 photon lifetimes, respectively. As expected, all three microcombs show high average visibility \bar{V} above 91% at zero photon lifetime. For one photon lifetime, \bar{V} remains above 83% for all states reported. At 3 photon lifetimes, \bar{V} starts to decrease to around 64%. Still, several comb lines maintain visibility fringes above 80% for all three microcombs, indicating high coherence and minimal noise for such lines^{70,72}. These results demonstrate the ability of our approach to target application-suitable microcomb states, such as for coherent communications³² and precise spectroscopy⁷³.

Additionally, Fig. 6 shows stability characterization measurements for a particular microcomb shape, reported in Fig. 3e. The main plot displays line-by-line stability in terms of the standard deviation. The stability measurement exhibits minimal variation in the comb line peaks, with a standard deviation value below 0.1 for all frequencies, over one day. The inset of Fig. 6 illustrates power transmission as the pump laser is scanned to generate the microcomb. We note a distinct drop in power associated with SC formation within the trace, as widely reported⁷⁴.

Microcomb modelling

We apply the formalism of the Lugiato-Lefever equation⁷⁵ (LLE) to describe microcomb dynamics generated by our GA and provide a preliminary understanding of the feasibility of the targeted output regimes. The evolution of the field in MRRs driven by an external pump field is governed by:

$$t_r \partial_t E(t, \tau) = \left(-\alpha - i\delta_{\omega_0} - L \frac{\beta_2}{2} \partial_\tau^2 + i\gamma L |E|^2 \right) E + \sqrt{k} F_{in}. \quad (5)$$

The LLE introduces a reference time $\tau \in [-t_r/2, t_r/2]$ that is related to the group velocity of the pump field F_{in} , a center frequency ω_0 , and a slow time t associated to the number of round-trips N , as $E(t = Nt_r, \tau)$. t_r is the round-trip time of the MRR, α represents the total system losses, δ_{ω_0} is the phase detuning of the pumping field with respect to ω_0 , L is the round-trip length, β_2 is the group velocity dispersion, and k is the coupling coefficient of the pump field, which considers the input losses. γ is the nonlinear parameter associated with the Kerr effect, which can be expressed as $\gamma = (\omega_0 n_2) / (cA_e)$, where A_e is the effective nonlinear mode area of the MRR waveguide while n_2 is the Kerr refractive index. Considering the MRR sample in our scheme, the parameters for the simulations are set to $t_r = 22\text{ps}$, $L = 592\mu\text{m}$, $\beta_2 = -10\text{ps}^2\text{km}^{-1}$, $\gamma = 220\text{W}^{-1}\text{km}^{-1}$, and $k=0.3$, while losses and higher-order dispersion terms are neglected. With such values, we sweep the detuning δ_{ω_0} around ω_0 at a speed $d\omega/dt$, and setting the average power of the field F_{in} , $P_{F_{in}} = 1.8\text{W} - 2.1\text{W}$, compatibly with the GA parameter I . Given the large intra-cavity field intensity in the MRR, we neglect any thermal-induced resonance drift term in the equation^{15,69}. However, our GA accounts for and counterbalances this effect.

Figure 7a and b display simulation results for two exemplary microcombs: a multi-soliton state and a stable MI microcomb state, corresponding to the cases shown in Fig. 3c and d. The exact alignment of the spectral traces underscores consistency between experimental and simulated results. The simulated temporal profiles of the intracavity fields, depicted as insets in Fig. 7, offer insights into the nature of these two regimes. The temporal trace in the inset of Fig. 7a reveals a structure consistent with multi-soliton bound states⁷⁶, previously demonstrated in microresonators⁷⁷, characterized by sub-picosecond components and spaced by 0.22 ps. The inset in Fig. 7b depicts pulse profiles interspersed with secondary modulated fringes, closely resembling the characteristics of a stable MI microcomb⁷⁸.

Discussion

Our work proposes a smart scheme to target distinct microcomb regimes via GAs for various real-world applications. Given the modular aspect of the fitness function that we employ in our scheme, our smart approach is highly versatile and applicable to other devices for microcomb generation, including (micro) cavities with different geometries and materials (e.g., silicon-based platforms), highly nonlinear fibers, and spiral waveguides⁷⁹, that feature a third-order nonlinear response to the propagating electrical field (e.g., two-photon absorption). This is due to the model-free nature of our implementation, requiring minimal information on the geometry and properties of the specific waveguide.

In addition, our approach is straightforwardly adaptable to different setup configurations for microcomb generation involving additional components, such as for multiple laser sources⁸⁰, as well as other tuning mechanisms (e.g., multi-stage scanning or back scanning). In such cases, adapting the GA amounts to introducing new objectives in Eq. 2, whose arguments are associated with the new components' parameters. Similarly, we can include additional constraints defining the target microcombs that introduce new degrees of freedom to the fitness function, in turn tailoring the microcombs towards specific applications. For example, in telecommunications where it is essential to mitigate microcomb noise, an objective can be included in Eq. 2 to account for noise characteristics during the optimization. In Fig. 2d we observe a flat microcomb, reaching a spectral flatness of $\pm 3\text{dBm}$ that fills the C-band of telecommunication (from 190 THz to 196 THz). Thus, our smart scheme is a promising alternative for telecommunication and machine learning applications where current

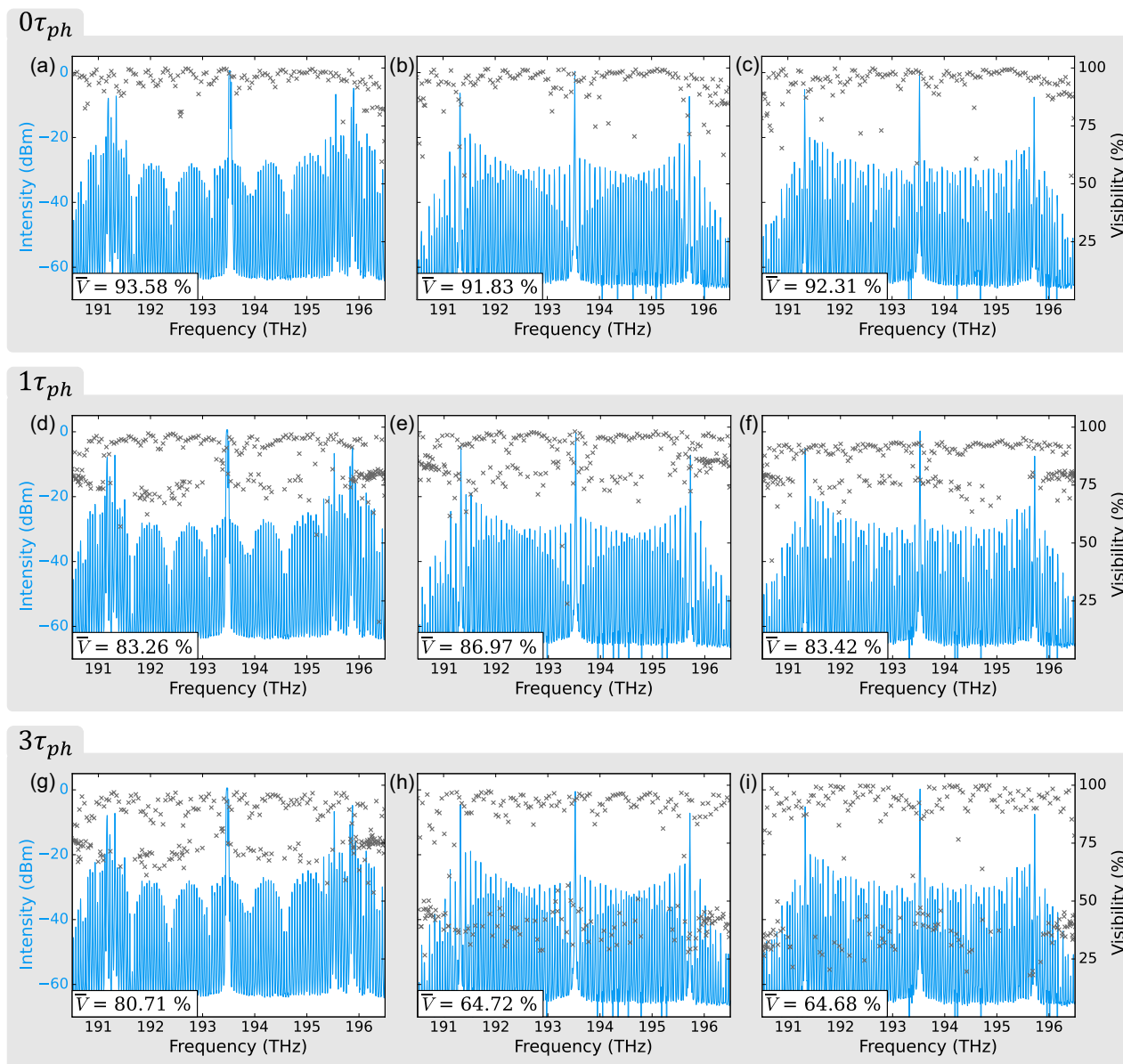


Fig. 5 | Spectral coherence of microcombs. Gray scatter plots show the visibility calculated at each comb line as a measure of spectral coherence⁷⁰, to characterize microcomb shapes located by the genetic algorithm at **a–c** 20 ps delay ($\sim 0\tau_{ph}$),

d–f 5 ns delay ($\sim 1\tau_{ph}$), and **g–i** 15 ns ($\sim 3\tau_{ph}$), respectively, for each presented microcomb state. Each panel is also labelled with the average visibility value \bar{V} as an inset.

implementations require expensive spectral shapers to achieve flat microcomb spectra^{4,81}.

Furthermore, the experimentally obtained microcombs have shown stability in their spectral features over a period of 12 hours to 1 day, overall extending previous results in the same direction^{48,82}.

In Fig. 3, we demonstrate that our scheme can find optimal combinations of the input parameters that reproduce microcomb spectral envelopes with profiles corresponding to distinct complex comb dynamics, including SCs and multi-soliton states.

We note that our results are reproducible in the sense that, once the optimal set of parameters for a target microcomb shape has been located by the GA, we can reproduce the exact same output by directly inputting these parameters to the experimental setup. Indeed, this has been further demonstrated as we subsequently generated the same output microcombs when performing additional coherence and stability measurements. Moreover, the states that we obtain using the optimized parameters are stable against external perturbations (Fig. 6), such as mechanical vibrations, temperature instabilities,

and other environmental factors. Together with the reproducibility claim of our results, our measurements prove the high robustness of our scheme.

In comparison with exhaustive search methods using standard sweeping approaches, which are limited in their ability to explore a large or complex solution space and are sensitive to noise and measurement errors, our proposed scheme is time- and resource-efficient with significant benefits towards real-world applications, as we quantitatively report in Fig. 4. The use of GAs drastically reduces the need for time-consuming and labor-intensive trial-and-error experiments to find a desired microcomb. It can quickly explore a large parameter space to identify the optimal input parameters that lead to the best performance.

The microcombs obtained by our smart approach can be numerically reproduced using the well-established theoretical framework of the LLE, as shown in the exemplary cases reported in Fig. 7, which can offer a preliminary understanding on the feasibility of the targeted states. On the other hand, the realization of complex spectral envelopes that would be otherwise difficult to predict numerically (e.g., due to model complexity limiting the

accuracy and resource consumption of numerical simulation), are, instead, experimentally obtainable with this scheme as shown in Fig. 3.

Conclusions

Our work demonstrates a smart approach for locating and generating distinct, specific microcomb states according to their desired intracavity power and spectral profiles. Our approach exhibits remarkable stability under external perturbations, and user-friendly reproducibility of the located microcombs.

Our findings have significant implications for developing portable, highly precise microcombs that can function robustly in uncontrolled environments. Indeed, our approach eliminates the need for additional stabilization mechanisms, thereby facilitating the utilization of microcomb dynamics across a broad range of out-of-lab applications. With the precise control of individual microcomb lines offered by GA, we can exploit individual frequency components to achieve ultra-dense, broadband data encoding for optical signal processing. This can improve existing spectral tailoring techniques, and enable the realization of photonic artificial neural networks. These advances open new avenues for real-time processing in

high-capacity communication networks, providing significant advantages over current methods.

Methods

Experimental setup for microcomb generation

We generate our microcombs in a four-port doped silica glass MRR⁶³, with an FSR of 48.9 GHz and featuring low linear loss (~ 0.06 dB cm^{-1}) and nonlinearity (~ 220 W $^{-1}$ km $^{-1}$), operating in the anomalous dispersion regime, with a group velocity dispersion $\beta_2 = -3.1$ ps 2 km $^{-1}$ TM and -10 ps 2 km $^{-1}$ TE mode at 193 THz. The MRR exhibits a mode crossing around 1552 nm. In our experimental setup, the MRR is pumped by a tunable CWL source (Santec TSL-710) that is amplified from 20 mW to ~ 1.8 W by an EDFA (Pritel PMFA-33), as shown in Fig. 1a. The MRR is mounted on a commercial thermoelectric cooler (TEC), to maintain the chip temperature near 30 °C.

Genetic algorithm parameters

The GA used in this study is based upon the open-source Python library ‘geneticalgorithm’⁸³. The library’s source code was modified to tailor the algorithm towards the microcomb generation task in this work. In particular, the crossover and parent selection operations were customized. The fitness function and multi-objective formulation of the optimization problem were fully developed for this work.

Following established approaches in evolutionary-based optimization techniques, we set the hyperparameters of the GA based upon preliminary manual exploration of the microcomb generation procedure, accounting for the trade-off between convergence time and quality of solution. As such, we set a population size of 20 individuals, a 20% mutation probability, a 50% crossover probability, and a 1% elitism ratio. The elitism ratio defines the portion of high-quality individuals allowed to continue ‘as-is’ to the next generation to retain the best-performing individuals within the gene pool. Furthermore, we select the parents according to a ‘roulette wheel’ approach, where higher quality candidates have a better chance of being selected as parents. Finally, we also utilize uniform crossover, where each gene is chosen from either parent with equal probability (as opposed to other mixing ratios, such as one- or two-point crossover, which would favour inheritance from one parent over another)⁸⁴. Each realization of the GA takes around 12 hours, although the total time includes the hardware-related bottlenecks (e.g., time required to scan and poll the OSA over GPIB connections was around 1 minute per scan, with each generation requiring hundreds of scans).

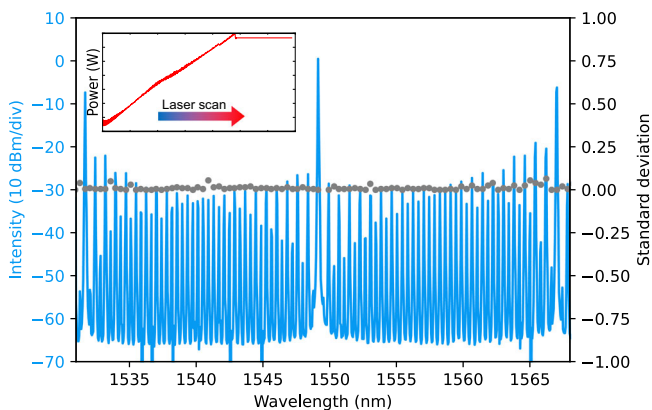


Fig. 6 | Stability of generated microcomb. Grey dots show the standard deviation of intensity value per comb line, measured over one day. The microcomb state (blue) is reproduced using the optimized parameters located by the GA. The inset shows the recorded power transmission trace at the through port of the MRR as the laser frequency is scanned to reproduce the microcomb, clearly showing the step-in power associated with SCs, as specified in the fitness function during the GA search.

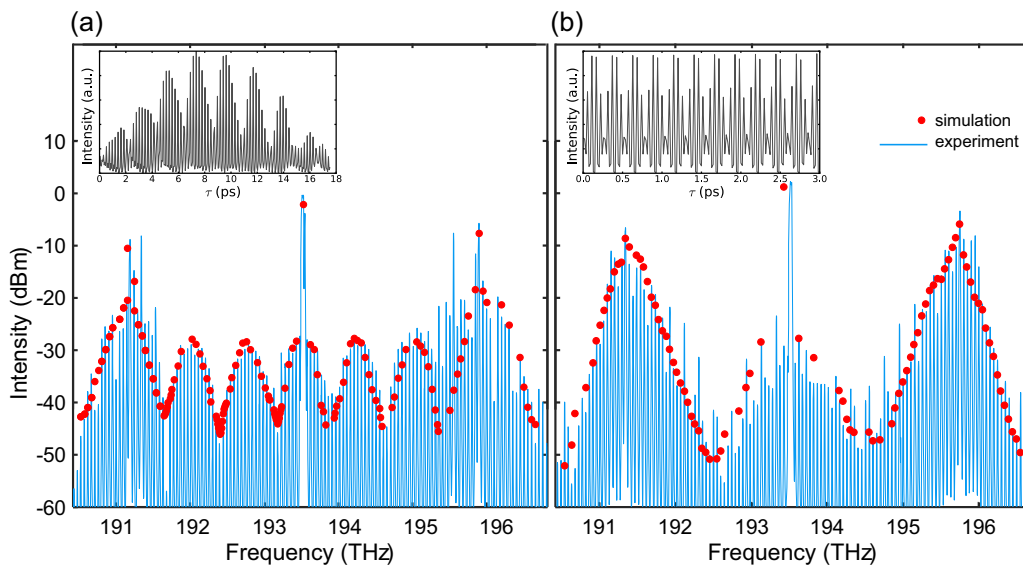


Fig. 7 | Microcomb modelling. Simulation results, represented by the red dots, fit exemplary microcombs obtained experimentally through the GA (solid blue line) for (a) the multisoliton regime and (b) the near MI regimes. Insets show the simulated temporal intra-cavity fields for each microcomb.

Our implementation also sets boundaries for the gene values as dictated by the specifications of the equipment and minimal knowledge of the system: the centre wavelength for the pump is limited between 1539 nm and 1552 nm, corresponding to the known range of the microring in which resonances near the mode crossing occur. The pump scan span boundaries are limited to approximately the width of a single MRR resonance linewidth. The upper limit of the step size for the laser scan is set similarly, while the lower limit is set to the laser step resolution, yielding a final range of 0.0001 nm - 0.005 nm. The limits on the dwell time are set based on those of the laser itself when in scan mode, from 0.1 s to 0.5 s. Finally, the EDFA current is limited to within its specification range, between 0.1 A and 4.2 A.

Our laser allows for two different scan modes, discrete and continuous. We performed our experiment using discrete scan steps according to the specified values for step size, span, and dwell time. The choice of discrete over continuous sweeping was motivated by the lower range in the scan speed provided by the laser in the continuous scan mode. In principle, with better equipment, continuous scanning can also be incorporated into our approach.

Choice of the fitness function

To characterize the quality of each individual, we have to specify a fitness function. The choice of the fitness function is an open problem in the field of evolutionary algorithms, with the definition of the function depending on the specific targets of the optimization problem. Our fitness function for the microcomb generation and tailoring process, defined in Eq. (2), is characterized by some or all the following objectives, which specify the target spectrum criteria:

Target line spacing between microcomb lines. We tailor the line spacing of the microcomb by defining it as some multiple of the device's FSR (although an explicit value can also be specified). We measure the distance between consecutive intensity peaks in the spectral trace, average these measurements, and then apply a normalized Euclidean norm. This yields a value that indicates proximity to the target line spacing, as retrieved using the following formula:

$$\frac{|s_{target} - s|}{s_{target}}, \quad (6)$$

where s_{target} is the target line spacing and s is the measured average line spacing of the microcomb.

Uniformity of the microcomb line separation. This metric is implemented as a (normalized) standard deviation using the following relation:

$$\max\left(\frac{\sigma}{\mu}, C\right), \quad (7)$$

where μ is mean spacing, σ is the standard deviation of the measured distances between adjacent comb lines, and C is an empirically defined ceiling value (to keep the value within bounds).

We collect the spectral traces with the OSA set to maximum hold mode, at the end of each laser scan, while the OSA is scanning during the microcomb generation procedure. The max-hold trace illustrates the comb shape achieved even if the laser steps too far and overshoots the microcomb state (e.g., the sweep span parameter is too wide). In such a way, combined with the power trace criterion (see below), we monitor the microcomb shapes achieved even when they are overshoot.

Envelope general uniformity and proximity to a defined shape. The peaks of each line are interpolated together, then a Euclidian norm is applied to find the distance from the target shape, analogous to Eq. (6). If no target shape is defined, then the score is based on the standard deviation of adjacent peak heights, analogous to Eq. (7), to target a

smooth intensity transition between adjacent microcomb lines. This latter metric avoids general chaotic states, whereas the former targets specific shapes. An explicit definition of a target shape is a stricter criterion and requires knowledge of the possible microcomb states, whereas the uniformity criterion is better suited for a simple exploration of non-chaotic regimes. In this way, we indirectly impose an intensity-related objective without setting a large number of targets for each microcomb line.

Power trace. We track the microcomb evolution through the power trace – for example, the MRR exhibits a threshold intracavity power level for comb formation, while a distinct drop in power is measured when the comb state is lost (i.e., the comb is unstable or overshoot). Furthermore, some microcomb states (e.g., SCs) are associated with distinct features in the power trace corresponding to the dynamical regime in which they form^{62,67,85}. We assign a penalty function associated with the power trace: a sudden, very large, drop signifies a lost state and, thus, we assign a penalty whose value is related to where the drop occurs. In the case of distinct features with respect to the power trace, the penalty is assigned if the desired features are not found in the trace. The penalty is then added to the overall fitness score. If the desired power criterion is not met, the overall fitness score is worse, thus encouraging the algorithm to find regimes that fulfill this criterion.

Thus, for any single realization of the GA, a combination of the above four criteria is used to specify the type of microcomb desired as the target. Since we define the total fitness function as a weighted sum of multiple objectives, skewing the weightings allows for favoring specific objectives (or, by implication, microcomb features) over others depending on the use case. If an objective is not relevant – that is, no constraint on that specific criterion is needed for the intended microcomb – a zero-weight assignment to said objective allows us to eliminate it. In this way, we ensure maximum reconfigurability in our algorithm.

We also account for auxiliary restrictions that need to be considered. For example, a 'death penalty' is assigned to individuals that are deemed as infeasible solutions – that is, the case of finding a single pump line at the end of the laser scan implies no microcomb formation occurred, and thus receives an extremely poor score to ensure it is not selected for the next generation and is quickly removed. We set boundaries on the values of the possible genes as dictated by equipment specifications and our understanding of the parameter space of the system (e.g., minimum required power for nonlinear processes to occur vs maximum input power allowed into the MRR).

Data availability

The data that support the plots of this paper and other findings within this study are available from the corresponding author upon reasonable request.

Code availability

The codes used for this study are available from the corresponding author upon reasonable request.

Received: 30 April 2023; Accepted: 12 February 2024;

Published online: 05 March 2024

References

1. Hänsch, T. W. Nobel Lecture: passion for precision. *Rev. Mod. Phys.* **78**, 1297–1309 (2006).
2. Diddams, S. A., Vahala, K. & Udem, T. Optical frequency combs: coherently uniting the electromagnetic spectrum. *Science* **369**, eaay3676 (2020).
3. Fortier, T. & Baumann, E. 20 years of developments in optical frequency comb technology and applications. *Commun. Phys.* **2**, 153 (2019).
4. Xu, X. et al. 11 TOPS photonic convolutional accelerator for optical neural networks. *Nature* **589**, 44–51 (2021).

5. Xu, X. et al. Photonic perceptron based on a Kerr Microcomb for high-speed, scalable, optical neural networks. *Laser Photonics Rev.* **14**, 2000070 (2020).
6. Bao, H. et al. Laser cavity-soliton microcombs. *Nat. Photonics* **13**, 384–389 (2019).
7. Rowley, M. et al. Self-emergence of robust solitons in a microcavity. *Nature* **608**, 303–309 (2022).
8. Moody, G. et al. Roadmap on integrated quantum photonics. *J. Phys. Photonics* **4**, 012501 (2022).
9. Reimer, C. et al. Generation of multiphoton entangled quantum states by means of integrated frequency combs. *Science* **351**, 1176–1180 (2016).
10. Kues, M. et al. On-chip generation of high-dimensional entangled quantum states and their coherent control. *Nature* **546**, 622–626 (2017).
11. Reimer, C. et al. High-dimensional one-way quantum processing implemented on d-level cluster states. *Nat. Phys.* **15**, 148–153 (2018).
12. Lesko, D. M. B. et al. A six-octave optical frequency comb from a scalable few-cycle erbium fibre laser. *Nat. Photonics* **15**, 281–286 (2021).
13. Kim, Y.-J., Chun, B. J., Kim, Y., Hyun, S. & Kim, S.-W. Generation of optical frequencies out of the frequency comb of a femtosecond laser for DWDM telecommunication. *Laser Phys. Lett.* **7**, 522–527 (2010).
14. Manurkar, P. et al. Fully self-referenced frequency comb consuming 5 watts of electrical power. *OSA Contin.* **1**, 274 (2018).
15. Pasquazi, A. et al. Micro-combs: A novel generation of optical sources. *Phys. Rep.* **729**, 1–81 (2018).
16. Gaeta, A. L., Lipson, M. & Kippenberg, T. J. Photonic-chip-based frequency combs. *Nat. Photonics* **13**, 158–169 (2019).
17. Sun, Y. et al. Applications of integrated optical microcombs. *Adv. Opt. Photonics* **15**, 86 (2023).
18. Pasquazi, A. et al. Self-locked optical parametric oscillation in a CMOS compatible microring resonator: a route to robust optical frequency comb generation on a chip. *Opt. Express* **21**, 13333 (2013).
19. Turitsyn, S. K., Bednyakova, A. E., Fedoruk, M. P., Papernyi, S. B. & Clements, W. R. L. Inverse four-wave-mixing and self-parametric amplification effect in optical fibre. *Nat. Photonics* **9**, 608–614 (2015).
20. Di Lauro, L. et al. Parametric control of thermal self-pulsation in microcavities. *Opt. Lett.* **42**, 3407 (2017).
21. Razzari, L. et al. CMOS-compatible integrated optical hyper-parametric oscillator. *Nat. Photonics* **4**, 41–45 (2010).
22. Reimer, C. et al. Cross-polarized photon-pair generation and bi-chromatically pumped optical parametric oscillation on a chip. *Nat. Commun.* **6**, 8236 (2015).
23. Pasquazi, A. et al. All-optical wavelength conversion in an integrated ring resonator. *Opt. Express* **18**, 3858–3863 (2010).
24. Suh, M. G. & Vahala, K. J. Soliton microcomb range measurement. *Science* **359**, 884–887 (2018).
25. Papp, S. B. et al. Microresonator frequency comb optical clock. *Optica* **1**, 10–14 (2014).
26. Ulanov, A. E. et al. Synthetic-reflection self-injection-locked microcombs. (2023).
27. Xu, X. et al. Photonic perceptron based on a Kerr microcomb for high-speed, scalable, optical neural networks. In *2020 International Topical Meeting on Microwave Photonics (MWP)* 220–224 (IEEE, 2020).
28. Borghi, M., Biasi, S. & Pavesi, L. Reservoir computing based on a silicon microring and time multiplexing for binary and analog operations. *Sci. Rep.* **11**, 15642 (2021).
29. Vaidya, S., Ambad, P. & Bhosle, S. Industry 4.0 – A Glimpse. *Procedia Manuf.* **20**, 233–238 (2018).
30. Jin, L. et al. Optical multi-stability in a nonlinear high-order microring resonator filter. *APL Photonics* **5**, 56106 (2020).
31. Geng, Y. et al. Coherent optical communications using coherence-cloned Kerr soliton microcombs. *Nat. Commun.* **13**, 1070 (2022).
32. Pfeifle, J. et al. Coherent terabit communications with microresonator Kerr frequency combs. *Nat. Photonics* **8**, 375–380 (2014).
33. Jørgensen, A. A. et al. Petabit-per-second data transmission using a chip-scale microcomb ring resonator source. *Nat. Photonics* **16**, 798–802 (2022).
34. Corcoran, B. et al. Ultra-dense optical data transmission over standard fibre with a single chip source. *Nat. Commun.* **11**, 2568 (2020).
35. Wang, W. et al. Dual-pump Kerr Micro-cavity Optical Frequency Comb with varying FSR spacing. *Sci. Rep.* **6**, 28501 (2016).
36. Del’Haye, P., Papp, S. B. & Diddams, S. A. Hybrid Electro-Optically Modulated Microcombs. *Phys. Rev. Lett.* **109**, 263901 (2012).
37. Lihachev, G. V. et al. Laser Self-Injection Locked Frequency Combs in a Normal GVD Integrated Microresonator. In *Conference on Lasers and Electro-Optics (2020)*, paper STh1O.3 STh1O.3 (Optica Publishing Group, 2020).
38. Peccianti, M. et al. Demonstration of a stable ultrafast laser based on a nonlinear microcavity. *Nat. Commun.* **3**, 765 (2012).
39. Trocha, P. et al. Ultrafast optical ranging using microresonator soliton frequency combs. *Science* **359**, 887–891 (2018).
40. Delsanto, S., Griffa, M. & Morra, L. Inverse Problems and Genetic Algorithms. In *Universality of Nonclassical Nonlinearity: Applications to Non-Destructive Evaluations and Ultrasonic*. 349–366 (Springer, 2006).
41. Aster, R., Borchers, B. & Thurber, C. *Parameter Estimation and Inverse Problems*. (Elsevier, 2013).
42. Fischer, B. et al. Autonomous on-chip interferometry for reconfigurable optical waveform generation. *Optica* **8**, 1268 (2021).
43. Simon, D. *Evolutionary optimization algorithms: biologically-Inspired and population-based approaches to computer intelligence*. in (Wiley, 2013).
44. Michalewicz, Z. & Schoenauer, M. Evolutionary Algorithms for Constrained Parameter Optimization Problems. *Evol. Comput.* **4**, 1–32 (1996).
45. Yao, L. & Sethares, W. A. Nonlinear parameter estimation via the genetic algorithm. *IEEE Trans. Signal Process.* **42**, 927–935 (1994).
46. Galbally, J., Ross, A., Gomez-Barrero, M., Fierrez, J. & Ortega-Garcia, J. Iris image reconstruction from binary templates: An efficient probabilistic approach based on genetic algorithms. *Comput. Vis. Image Underst.* **117**, 1512–1525 (2013).
47. De Carvalho Filho, A. O., Silva, A. C., De Paiva, A. C., Nunes, R. A. & Gattass, M. Computer-aided diagnosis system for lung nodules based on computed tomography using shape analysis, a genetic algorithm, and SVM. *Med. Biol. Eng. Comput.* **55**, 1129–1146 (2017).
48. Zhang, C., Kang, G., Wang, J., Pan, Y. & Qu, J. Inverse design of soliton microcomb based on genetic algorithm and deep learning. *Opt. Express* **30**, 44395–44407 (2022).
49. Pal, A., Ghosh, A., Zhang, S., Bi, T. & Del’Haye, P. Machine learning assisted inverse design of microresonators. *Opt. Express* **31**, 8020–8028 (2023).
50. Ahn, G. H. et al. Photonic Inverse Design of On-Chip Microresonators. *ACS Photonics* **9**, 1875–1881 (2022).
51. Lucas, E., Yu, S.-P., Briles, T. C., Carlson, D. R. & Papp, S. B. Tailoring microcombs with inverse-designed, meta-dispersion microresonators. *Nat. Photonics* **17**, 943–950 (2023).
52. Minkov, M. et al. Inverse Design of Photonic Crystals through Automatic Differentiation. *ACS Photonics* **7**, 1729–1741 (2020).
53. Wang, Z., Ye, F. & Li, Q. Modified genetic algorithm for high-efficiency dispersive waves emission at 3 μm . *Opt. Express* **30**, 2711–2720 (2022).
54. Wu, X. et al. Farey tree and devil’s staircase of frequency-locked breathers in ultrafast lasers. *Nat. Commun.* **13**, 5784 (2022).
55. Wetzel, B. et al. Customizing supercontinuum generation via on-chip adaptive temporal pulse-splitting. *Nat. Commun.* **9**, 1–10 (2018).

56. Arteaga-Sierra, F. R. et al. Supercontinuum optimization for dual-soliton based light sources using genetic algorithms in a grid platform. *Opt. Express* **22**, 23686 (2014).
57. Zheng, P.-Z. et al. Autosetting soliton pulsation in a fiber laser by an improved depth-first search algorithm. *Opt. Express* **29**, 34684 (2021).
58. Girardot, J. et al. On-demand generation of soliton molecules through evolutionary algorithm optimization. *Opt. Lett.* **47**, 134–137 (2022).
59. Andral, U. et al. Toward an autosetting mode-locked fiber laser cavity. *JOSA B* **33**, 825–833 (2016).
60. Woodward, R. I. & Kelleher, E. J. R. Towards ‘smart lasers’: self-optimisation of an ultrafast pulse source using a genetic algorithm. *Sci. Rep.* **6**, 37616 (2016).
61. Haelterman, M., Trillo, S. & Wabnitz, S. Dissipative modulation instability in a nonlinear dispersive ring cavity. *Opt. Commun.* **91**, 401–407 (1992).
62. Cole, D. C., Lamb, E. S., Del’Haye, P., Diddams, S. A. & Papp, S. B. Soliton crystals in Kerr resonators. *Nat. Photonics* **11**, 671–676 (2017).
63. Moss, D. J., Morandotti, R., Gaeta, A. L. & Lipson, M. New CMOS-compatible platforms based on silicon nitride and Hydex for nonlinear optics. *Nat. Photonics* **7**, 597–607 (2013).
64. Del’Haye, P. et al. Optical frequency comb generation from a monolithic microresonator. *Nature* **450**, 1214–1217 (2007).
65. Brasch, V. et al. Photonic chip-based optical frequency comb using soliton Cherenkov radiation. *Science* **351**, 357–360 (2016).
66. Kippenberg, T. J., Gaeta, A. L., Lipson, M. & Gorodetsky, M. L. Dissipative Kerr solitons in optical microresonators. *Science* **361**, eaan8083 (2018).
67. Herr, T. et al. Temporal solitons in optical microresonators. *Nat. Photonics* **8**, 145–152 (2014).
68. *Dissipative Optical Solitons*. vol. 238 (Springer International Publishing, 2022).
69. Carmon, T., Yang, L. & Vahala, K. J. Dynamical thermal behavior and thermal self-stability of microcavities. *Opt. Express* **12**, 4742 (2004).
70. Webb, K. E. et al. Measurement of microresonator frequency comb coherence by spectral interferometry. *Opt. Lett.* **41**, 277–280 (2016).
71. Webb, K. E., Erkintalo, M., Coen, S. & Murdoch, S. G. Experimental observation of coherent cavity soliton frequency combs in silica microspheres. *Opt. Lett.* **41**, 4613 (2016).
72. Derickson, D. *Fiber Optic Test and Measurement*. (Prentice Hall PTR, 1998).
73. Bao, C. et al. Architecture for microcomb-based GHz-mid-infrared dual-comb spectroscopy. *Nat. Commun.* **12**, 6573 (2021).
74. Karpov, M. et al. *Dynamics of soliton crystals in optical microresonators*. 2017 Conference on Lasers and Electro-Optics, CLEO 2017 - Proceedings vols 2017-Janua (OSA, 2017).
75. Lugiato, L. A. & Lefever, R. Spatial Dissipative Structures in Passive Optical Systems. *Phys. Rev. Lett.* **58**, 2209–2211 (1987).
76. Tang, D. Y., Zhao, L. M. & Zhao, B. Multipulse bound solitons with fixed pulse separations formed by direct soliton interaction. *Appl. Phys. B* **80**, 239–242 (2005).
77. Cutrona, A. et al. Nonlocal bonding of a soliton and a blue-detuned state in a microcomb laser. *Commun. Phys.* **6**, 1–10 (2023).
78. Erkintalo, M. & Coen, S. Coherence properties of Kerr frequency combs. *Opt. Lett.* **39**, 283–286 (2014).
79. Duchesne, D. et al. Efficient self-phase modulation in low loss, high index doped silica glass integrated waveguides. *Opt. Express* **17**, 1865 (2009).
80. Lu, Z. et al. Synthesized soliton crystals. *Nat. Commun.* **12**, 3179 (2021).
81. Del’Haye, P. et al. Phase steps and resonator detuning measurements in microresonator frequency combs. *Nat. Commun.* **6**, 5668 (2015).
82. Pinto, T. et al. Optimization of frequency combs spectral-flatness using evolutionary algorithm. *Opt. Express* **29**, 23447–23460 (2021).
83. Solgi, R. *Python Package for Genetic Algorithm (GA)*. <https://doi.org/10.5281/zenodo.3784414> (2020).
84. Syswerda, G. Uniform Crossover in Genetic Algorithms. In *Proceedings of the 3rd International Conference on Genetic Algorithms 2–9* (Morgan Kaufmann Publishers Inc., 1989).
85. Guo, H. et al. Universal dynamics and deterministic switching of dissipative Kerr solitons in optical microresonators. *Nat. Phys.* **13**, 94–102 (2017).

Acknowledgements

This work was supported by the Natural Sciences and Engineering Research Council of Canada (NSERC) through the Strategic, Discovery, and Alliance Grants Schemes, by the MEIE PSR-SIIRI Initiative in Quebec, and by the Canada Research Chair Program. This work was also supported by the Mitacs Elevate Postdoctoral Fellowship Program.

Author contributions

C.M. and L.D.L. contributed equally to this work. C.M. developed the algorithm, performed the experiments, and analyzed the data. L.D.L. conceived the idea, coordinated the execution of the project, and performed simulations. I.A. contributed to the experimental design and concept. N.P. contributed to the characterization of microcombs and participated in scientific discussions. S.T.C. designed the microring resonator while B.E.L. fabricated the chip. B.F., A.A., A.E., B.E.L., and D.J.M. contributed to scientific discussions. R.M. supervised the project. Every author contributed to the redaction of the paper.

Competing interests

The authors declare no competing interests.

Additional information

Correspondence and requests for materials should be addressed to Luigi Di Lauro or Roberto Morandotti.

Peer review information *Communications Physics* thanks Hao-Jing Chen and the other, anonymous, reviewer(s) for their contribution to the peer review of this work.

Reprints and permissions information is available at <http://www.nature.com/reprints>

Publisher’s note Springer Nature remains neutral with regard to jurisdictional claims in published maps and institutional affiliations.

Open Access This article is licensed under a Creative Commons Attribution 4.0 International License, which permits use, sharing, adaptation, distribution and reproduction in any medium or format, as long as you give appropriate credit to the original author(s) and the source, provide a link to the Creative Commons licence, and indicate if changes were made. The images or other third party material in this article are included in the article’s Creative Commons licence, unless indicated otherwise in a credit line to the material. If material is not included in the article’s Creative Commons licence and your intended use is not permitted by statutory regulation or exceeds the permitted use, you will need to obtain permission directly from the copyright holder. To view a copy of this licence, visit <http://creativecommons.org/licenses/by/4.0/>.

© The Author(s) 2024